Key Points:
- A general algorithm for linear and quadratic gradients based on 10 or more spacecraft measurements is presented for the first time
- The characteristic matrix of the constellation affecting the determination of the quadratic gradient is found and its features demonstrated
- The algorithm is confirmed with tests on magnetic fields, indicating that the linear magnetic gradient obtained is of second-order accuracy

Supporting Information:

Supporting Information may be found in the online version of this article.

Correspondence to:

C. Shen,
shenchao@hit.edu.cn

A General Algorithm for the Linear and Quadratic Gradients of Physical Quantities Based on 10 or More Point Measurements

Chao Shen[1] , Yufei Zhou[1] , Yonghui Ma[1] , Xiaogang Wang[2], Zuyin Pu[3] , and M. Dunlop[4,5]

[1]School of Science, Harbin Institute of Technology, Shenzhen, China, [2]School of Physics, Harbin Institute of Technology, Harbin, China, [3]School of Earth and Space Sciences, Peking University, Beijing, China, [4]School of Space and Environment, Beihang University, Beijing, China, [5]Rutherford Appleton Laboratory, Chilton, DIDCOT, Oxfordshire, UK

Abstract A novel algorithm for estimating both the linear and quadratic gradients of physical quantities based on multiple spacecraft observations using the least squares method is put forward. Using 10 or more spacecraft constellation measurements as input, this new algorithm can yield both the linear and quadratic gradients at the barycenter of the constellation. Iterations were used in the algorithm. Tests on cylindrical flux ropes, dipole magnetic field, and modeled geomagnetospheric field were carried out. The results of these tests indicate that the linear gradient obtained is of second-order accuracy, while the quadratic gradient is of first-order accuracy. The test on the modeled geomagnetospheric field showed that, the greater the number of spacecraft in the constellation, the greater the accuracy of the quadratic gradient calculated. However, the accuracy of the linear gradient obtained was independent of the number of spacecraft. The feasibility, reliability, and accuracy of this algorithm have been successfully verified. This algorithm could find wide applications in the design of future multiple spacecraft missions as well as in the analysis of multiple-point measurement data.

Plain Language Summary As space exploration develops, constellations of 10 or more spacecraft may become a reality in the near future. However, there is still no general mathematical algorithm for calculating the second-order or quadratic gradient of various physical quantities using 10 or more point measurements. In this paper, we present a universal approach that can estimate both the linear and the quadratic gradients of physical quantities based on 10 or more point measurements. This algorithm has been tested and its reliability verified. The results of these tests show that the linear gradient obtained is of second-order accuracy, while the quadratic gradient is of first-order accuracy. This new algorithm will aid the design of future multiple spacecraft missions and will have wide application in analyzing multiple-point measurement data.

1. Introduction

The gradients of physical quantities play important roles in the dynamic evolution of space plasmas. For example, the first-order gradient of electromagnetic fields balances their temporal variations as well as their sources (charge density and current density); the linear gradient of certain physical quantities (magnetic field, thermal pressure, etc.) can also drive the drift motions of charged particles in electromagnetic fields. The linear gradient of physical quantities can be estimated from 4-point in-situ measurements with first-order accuracy, and many estimators have already been developed (Chanteur, 1998; De Keyser, 2008; De Keyser, et al., 2007; Dunlop et al., 1988; Hamrin et al., 2008; Harvey, 1998; Vogt et al., 2008, 2009).

On the other hand, the quadratic gradients of physical quantities can lead to diffusion and dissipation processes in plasmas. The quadratic gradients of electromagnetic potentials can balance the sources as shown by the Poisson equation. The geometry of the magnetic field depends on both the first-order and second-order magnetic gradients (Shen et al., 2020).

Recently several investigations have been made to fit the magnetic field to the second-order, based on four spacecraft magnetic and current density observations (Liu et al., 2019; Torbert et al., 2020). Shen

et al. (2020) have put forward an explicit algorithm to calculate the quadratic magnetic gradient as well as the complete geometry of magnetic field lines with four point magnetic field and particle/current density measurements under the constraints of electromagnetic laws. This method has been successfully applied to analyze one flux rope event as observed by MMS (Burch et al., 2016; Pollock et al., 2016; Russell et al., 2016; Shen et al., 2020). These approaches, however, cannot be applied to estimate the quadratic gradients of other physical fields, such as those of density, temperature, electric potential, etc. Generally, at least 10 measurement points of a physical quantity are required to calculate its second-order gradient (Chanteur, 1998).

With the development of space exploration, constellation missions with 10 or more spacecraft have become possible (e.g., the Cross-Scale mission). However, we still do not have an applicable universal algorithm for estimating the quadratic gradients of physical quantities with 10 and more point measurements.

In this paper, we present a universal algorithm that can estimate both the linear and quadratic gradients of physical quantities based on 10 or more point measurements. This algorithm has been tested and its reliability verified. The accuracy of this algorithm has also been investigated. The algorithm is presented in Section 2, the tests of the method are described in Section 3, and a summary and discussion of the results are presented in Section 4.

2. The Algorithm

Consider that a constellation, composed of $N \geq 10$ spacecraft, performs in-situ observations on a certain physical field f (density, magnetic field, electric potential, etc.). In the Earth central frame of reference (or other inertial frames of the investigator), the Cartesian coordinates are (x^1, x^2, x^3) (corresponding to (x, y, z), respectively) with their bases as $(\hat{\mathbf{x}}_1, \hat{\mathbf{x}}_2, \hat{\mathbf{x}}_3)$. The position of the αth spacecraft is at $x_{(\alpha)}^i = \left(x_{(\alpha)}^1, x_{(\alpha)}^2, x_{(\alpha)}^3 \right) \left(\alpha = 1, 2, \cdots, N \right)$, and its velocity in the Earth-centered frame of reference is $\mathbf{u}_{(\alpha)}$. The coordinates x_c^i of the barycenter of the constellation satisfy Equation 1:

$$\sum_{\alpha=1}^{N} \Delta x_{(\alpha)}^i = \sum_{\alpha=1}^{N} \left(x_{(\alpha)}^i - x_c^i \right) = 0, \tag{1}$$

so that

$$x_c^i = \frac{1}{N} \sum_{\alpha=1}^{N} x_{(\alpha)}^i. \tag{2}$$

The physical quantity observed is $f'\left(x_\alpha^i \right) = f'_{(\alpha)}$ in the spacecraft reference frame and $f\left(x_\alpha^i \right) = f_{(\alpha)}$ in the Earth center reference frame (a static frame of reference), respectively. There is a certain transformation relationship between $f'_{(\alpha)}$ and $f_{(\alpha)}$. For the magnetic field, $\mathbf{B}'_{(\alpha)} = \mathbf{B}_{(\alpha)}$. For the electric field, $\mathbf{E}'_{(\alpha)} = \mathbf{E}_{(\alpha)} + \mathbf{u}_{(\alpha)} \times \mathbf{B}_{(\alpha)}$. For the vector and scalar potentials, $\mathbf{A}'_{(\alpha)} = \mathbf{A}_{(\alpha)}$ and $\phi'_{(\alpha)} = \phi_{(\alpha)} - \mathbf{u}_{(\alpha)} \cdot \mathbf{A}_{(\alpha)}$. For the charge density and current density, $\rho'_{(\alpha)} = \rho_{(\alpha)}$ and $\mathbf{j}'_{(\alpha)} = \mathbf{j}_{(\alpha)} - \mathbf{u}_{(\alpha)}\rho_{(\alpha)}$.

In the Earth center reference frame, the linear gradient of the physical quantity f is $\left(\partial f / \partial x^i \right) = \nabla_i f$, and its quadratic gradient is $\left(\partial^2 f / \partial x^i \partial x^j \right) = \nabla_i \nabla_j f$. Based on Taylor expansion, the physical quantity observed, $f_{(\alpha)}$, can be expressed as Equation (3):

$$f_{(\alpha)} = f_c + \Delta x_{(\alpha)}^i \nabla_i f_c + \frac{1}{2} \Delta x_{(\alpha)}^i \Delta x_{(\alpha)}^j \nabla_i \nabla_j f_c, \tag{3}$$

where all the gradients with orders higher than 2 are neglected under the assumption that $\Delta x_{(\alpha)}^i$ $\left(\alpha = 1, 2, \cdots, N\right)$ are much less than the characteristic scale of the structures investigated. Thus, there are 10 parameters $(f_c, \left(\nabla_i f\right)_c, \left(\nabla_i \nabla_j f\right)_c)$ to be determined. Equation 3 can also be written as

$$f_{(\alpha)} = f_c + \Delta x_{(\alpha)}^i g_i + \frac{1}{2}\Delta x_{(\alpha)}^i \Delta x_{(\alpha)}^j G_{ij}, \tag{3'}$$

where the linear and quadratic gradients of the physical quantities at the barycenter are $g_i = \left(\nabla_i f\right)_c$ and $G_{ij} = \left(\nabla_i \nabla_j f\right)_c$, respectively. It is noted that $G_{ij} = G_{ji}$. Therefore, to obtain the 10 parameters (f_c, g_i, G_{ij}), observations by the constellation with at least 10 spacecraft are required.

In order to obtain the estimator for the 10 parameters (f_c, g_i, G_{ij}) with the desired accuracy from the $N \geq 10$ spacecraft in-situ observations, we make use of the least squares method (Harvey, 1998; Shen et al., 2003). Assume the action to be

$$S = \frac{1}{N}\sum_\alpha \left[f_c + \Delta x_{(\alpha)}^i g_i + \frac{1}{2}\Delta x_{(\alpha)}^i \Delta x_{(\alpha)}^j G_{ij} - f_{(\alpha)} \right]^2. \tag{4}$$

Minimize this using

$$\delta S = 0. \tag{5}$$

so as to find the formulas for f_c, $g_i = \left(\nabla_i f\right)_c$ and $G_{ij} = \left(\nabla_i \nabla_j f\right)_c$.

Equation 5 leads to

$$\frac{\partial S}{\partial f_c} = 0, \; \frac{\partial S}{\partial g_i} = 0, \; \frac{\partial S}{\partial G_{ij}} = 0. \tag{6}$$

Because

$$\begin{aligned}\frac{\partial S}{\partial f_c} &= \frac{1}{N}\sum_{\alpha=1}^N 2\left[f_c + \Delta x_{(\alpha)}^i g_i + \frac{1}{2}\Delta x_{(\alpha)}^i \Delta x_{(\alpha)}^j G_{ij} - f_{(\alpha)} \right] \\ &= 2\cdot\frac{1}{N}\sum_{\alpha=1}^N \left[f_c - f_{(\alpha)} \right] + 2\cdot\frac{1}{N}\sum_{\alpha=1}^N \Delta x_{(\alpha)}^i g_i + \frac{1}{N}\sum_{\alpha=1}^N \Delta x_{(\alpha)}^i \Delta x_{(\alpha)}^j G_{ij} = 0,\end{aligned} \tag{7}$$

we get

$$f_c = \frac{1}{N}\sum_{\alpha=1}^N f_{(\alpha)} - \frac{1}{2N}\sum_{\alpha=1}^N \Delta x_{(\alpha)}^i \Delta x_{(\alpha)}^j G_{ij}, \tag{8}$$

where Equation 1 is used. Equation 8 can also be written as

$$f_c = \frac{1}{N}\sum_{\alpha=1}^N f_{(\alpha)} - \frac{1}{2} R^{ij} G_{ij}. \tag{8'}$$

Here, R^{ij} is the volumetric tensor (or 3×3 matrix) (Harvey, 1998; Shen et al., 2003), which is defined as

$$R^{ij} \equiv \frac{1}{N}\sum_{\alpha=1}^N \Delta x_{(\alpha)}^i \Delta x_{(\alpha)}^j = \frac{1}{N}\sum_{\alpha=1}^N \left(x_{(\alpha)}^i - x_c^i \right)\left(x_{(\alpha)}^j - x_c^j \right). \tag{9}$$

Therefore, the physical quantity at the barycenter is the average of all the measurements plus the correction term by the quadratic gradient.

From $\partial S / \partial g_i = 0$, we get

$$
\begin{aligned}
\frac{\delta S}{\delta g_i} &= \frac{1}{N}\sum_{\alpha=1}^{N} 2\left[f_c - f_{(\alpha)} + \Delta x_{(\alpha)}^k g_k + \frac{1}{2}\Delta x_{(\alpha)}^k \Delta x_{(\alpha)}^m G_{km} \right]\Delta x_{(\alpha)}^i \\
&= -2\frac{1}{N}\sum_{\alpha=1}^{N} f_{(\alpha)}\Delta x_{(\alpha)}^i + 2R^{ik}g_k + R^{ikm}G_{km} = 0,
\end{aligned}
\tag{10}
$$

where the third-order tensor is defined as

$$
R^{ikm} \equiv \frac{1}{N}\sum_{\alpha=1}^{N}\Delta x_{(\alpha)}^i \Delta x_{(\alpha)}^k \Delta x_{(\alpha)}^m.
\tag{11}
$$

R^{ikm} is symmetrical, i.e., $R^{ikm} = R^{kim} = R^{imk}$. Equation 10 reduces to

$$
R^{ik}g_k = \frac{1}{N}\sum_{\alpha}^{N}\left(x_{(\alpha)}^i - x_c^i \right)f_{(\alpha)} - \frac{1}{2}R^{ikm}G_{km}.
\tag{12}
$$

Let R^{-1} be the inverse of the volumetric tensor, which satisfies $\left(R^{-1}\right)_{ik}R^{kj} = R^{jk}\left(R^{-1}\right)_{ki} = \delta_i^j$. Hence, the linear gradient at the barycenter is obtained from Equation 12 as follows:

$$
g_i = \left(R^{-1}\right)_{ij} \cdot \frac{1}{N}\sum_{\alpha}^{N}\left(x_{(\alpha)}^j - x_c^j \right)f_{(\alpha)} - \frac{1}{2}\left(R^{-1}\right)_{ij}R^{jkm}G_{km}.
\tag{13}
$$

The second term on the right-hand side of the above Equation 13 is the correction arising from the quadratic gradient.

From $\partial S / \partial G_{ij} = 0$, we get

$$
\frac{\partial S}{\partial G_{ij}} = \frac{1}{N}\sum_{\alpha=1}^{N}\left[f_c - f_{(\alpha)} + \Delta x_{(\alpha)}^k g_k + \frac{1}{2}\Delta x_{(\alpha)}^k \Delta x_{(\alpha)}^m G_{km} \right]\Delta x_{(\alpha)}^i \Delta x_{(\alpha)}^j = 0.
\tag{14}
$$

Thus

$$
f_c R^{ij} - \frac{1}{N}\sum_{\alpha=1}^{N} f_{(\alpha)}\Delta x_{(\alpha)}^i \Delta x_{(\alpha)}^j + R^{ijk}g_k + \frac{1}{2}R^{ijkm}G_{km} = 0,
\tag{15}
$$

where the fourth-order tensor is

$$
R^{ijkm} \equiv \frac{1}{N}\sum_{\alpha=1}^{N}\Delta x_{(\alpha)}^i \Delta x_{(\alpha)}^j \Delta x_{(\alpha)}^k \Delta x_{(\alpha)}^m.
\tag{16}
$$

Note that R^{ijkm} is symmetric, with $R^{ijkm} = R^{jikm} = R^{ijmk} = R^{kmij}$. Obviously, f_c, $g_i = \left(\nabla_i f\right)_c$ and $G_{ij} = \left(\nabla_i \nabla_j f\right)_c$ can be obtained by solving Equations 8′, 12, and 15.

In order to ensure accurate calculations, we performed iterations to solve these equations, which can be conveniently realized by computation. First, a linear approximation is made with $G_{ij} = G_{ij}^{(0)} = 0$. Then, from Equations 8′ and 13, we obtain the physical quantity and its linear gradient at the barycenter as

$$
f_c^{(0)} = \frac{1}{N}\sum_{\alpha} f_{(\alpha)},
\tag{17}
$$

and

$$
g_i^{(0)} = \left(\nabla_i f\right)_c = \left(R^{-1}\right)_{ik}\frac{1}{N}\sum_{\alpha=1}^{N}\left(x_{(\alpha)}^k - x_c^k \right)f_\alpha,
\tag{18}
$$

respectively. Second, by substituting the above two equations into Equation 15, we can get

$$\frac{1}{2}R^{ijkm}G^{(1)}_{km} = \frac{1}{N}\sum_{\alpha=1}^{N}f_{(\alpha)}\Delta x^i_{(\alpha)}\Delta x^j_{(\alpha)} - R^{ij}f^{(0)}_c - R^{ijk}g^{(0)}_k, \tag{19}$$

with which the quadratic gradient $G^{(1)}_{km}$ at the first-order can be obtained. Substituting the first-order quadratic gradient $G^{(1)}_{km}$ into Equations 8′ and 13 to yield the physical quantity $f^{(1)}_c$ at the second-order and its linear gradient $g^{(1)}_i$ at the second-order, and, again, using Equation 15, we get the corrected quadratic gradient $G^{(2)}_{km}$ at the first-order from

$$\frac{1}{2}R^{ijkm}G^{(2)}_{km} = \frac{1}{N}\sum_{\alpha=1}^{N}f_{(\alpha)}\Delta x^i_{(\alpha)}\Delta x^j_{(\alpha)} - R^{ij}f^{(1)}_c - R^{ijk}g^{(1)}_k. \tag{19'}$$

Repeat the above processes to yield the solutions of Equations 8′, 12, and 15, i.e., the estimations of the 10 parameters $(f_c, \mathrm{g}_i = (\nabla_i f)_c, G_{ij} = (\nabla_i \nabla_j f)_c)$ of the plasma structure investigated.

Equation 15 is a tensor equation, whose concrete solution needs to be found. Rewriting it gives as follows:

$$\sum_{l=1}^{3}\sum_{k=1}^{3}R^{ijkl}G_{kl} = c^{ij}, \quad i,j = 1,2,3. \tag{20}$$

The tensor on the right-hand side of Equation 20 is defined as

$$c^{ij} \equiv \frac{2}{N}\sum_{\alpha=1}^{N}f_{(\alpha)}\Delta x^i_{(\alpha)}\Delta x^j_{(\alpha)} - 2R^{ij}f_c - 2R^{ijk}g_k. \tag{21}$$

We will transform the tensor Equation 20 into a matrix equation so as to obtain its solution concisely. The second-order tensor c^{ij} is symmetric, that is, $c^{ij} = c^{ji}$. c^{ij} contains six independent components, which can be expressed as $c^{(ij)} = \left(c^{11}, c^{12}, c^{13}, c^{22}, c^{23}, c^{33}\right)$. Similarly, the symmetric underdetermined tensor G_{ij} also contains six independent components, which can be written as $G_{(ij)} = \left(G_{11}, G_{12}, G_{13}, G_{22}, G_{23}, G_{33}\right)$. The fourth-order tensor R^{ijkl} is symmetric, and $R^{ijkl} = R^{(ij)(kl)}$, where both ij and kl have six independent compositions. Therefore, the tensor Equation 20 can be rewritten as

$$\sum_{l=k}^{3}\sum_{k=1}^{3}\left(2 - \delta_{kl}\right)R^{ijkl}G_{kl} = c^{ij}, \quad \left(i = 1,2,3, \ j = i,\cdots,3\right). \tag{22}$$

To facilitate the calculation, the coefficient on the left-hand side of Equation 22 should be index symmetric. Multiplying the two sides of Equation 22 by $\left(2 - \delta_{ij}\right)$ to yield

$$\sum_{l=k}^{3}\sum_{k=1}^{3}\left(2 - \delta_{ij}\right)\left(2 - \delta_{kl}\right)R^{ijkl}G_{kl} = \left(2 - \delta_{ij}\right)c^{ij}, \quad \left(i = 1,2,3, \ j = i,\cdots,3\right). \tag{23}$$

Note that in the above equation the sums over the indices i and j are not made even if i and j are repeated. Equation 23 can be regarded as a matrix equation in a six-dimensional space. The bases of this six-dimensional space are $(\hat{x}_1\hat{x}_1, \hat{x}_1\hat{x}_2, \hat{x}_1\hat{x}_3, \hat{x}_2\hat{x}_2, \hat{x}_2\hat{x}_3, \hat{x}_3\hat{x}_3)$, which can also be marked as $\left(\hat{k}_1, \hat{k}_2, \cdots, \hat{k}_6\right)$, or $\hat{k}_M$, $M = 1$, 2, ..., 6, satisfying $\hat{k}_M \cdot \hat{k}_N = \delta_{MN}$. The underdetermined tensor G_{ij}, which is composed of six independent components, can be treated as a vector in the six-dimensional space and written as $\mathbf{G} = \left(X^1, X^2, \cdots, X^6\right)$ with its components

$$X^M = G_{(kl)}. \tag{24}$$

$\mathbf{G}$ can be expressed in vector format as

$$\mathbf{G} = \sum_{M=1}^{6} X^M \hat{\mathbf{k}}_M. \tag{24'}$$

The term $\left(2 - \delta_{ij}\right)c^{ij}$ on the right-hand side of Equation 23 is composed of six components, and can also be regarded as a vector in the six-dimensional space and expressed as $\mathbf{C} = \left(C^1, C^2, \cdots, C^6\right)$, with the components

$$C^M = \left(2 - \delta_{ij}\right)c^{(ij)}. \tag{25}$$

Thus, the vector $\mathbf{C}$ in the six-dimensional space is written as

$$\mathbf{C} = \sum_{M=1}^{6} C^M \hat{\mathbf{k}}_M. \tag{26}$$

At the same time, the coefficient tensor $\left(2 - \delta_{ij}\right)\left(2 - \delta_{kl}\right)R^{ijkl}$ can be treated as a 6×6 matrix:

$$\mathfrak{R}^{MN} \equiv \left(2 - \delta_{ij}\right)\left(2 - \delta_{kl}\right)R^{(ij)(kl)}. \tag{27}$$

The index M corresponds to (ij), and N to (kl). The matrix $\mathfrak{R}^{MN}$ is symmetric and $\mathfrak{R}^{MN} = \mathfrak{R}^{NM}$, which can be expressed in vector format as

$$\mathfrak{R} = \mathfrak{R}^{MN} \hat{\mathbf{k}}_M \hat{\mathbf{k}}_N. \tag{28}$$

Like the 3×3 volumetric matrix R^{ij}, the 6×6 matrix $\mathfrak{R}^{MN}$ respects the characteristic geometric features of the constellation.

Therefore, the tensor Equation 20 has been transformed into a matrix equation as follows:

$$\mathfrak{R}^{MN} \cdot X^N = C^M. \tag{29}$$

whose vector form is

$$\mathfrak{R} \cdot \mathbf{G} = \mathbf{C}. \tag{29'}$$

The symmetric matrix $\mathfrak{R}^{MN}$ can be diagonalized. Suppose that its eigenvectors are $\left(\hat{\mathbf{e}}_1, \hat{\mathbf{e}}_2, \cdots, \hat{\mathbf{e}}_6\right)$, with $\hat{\mathbf{e}}_M \cdot \hat{\mathbf{e}}_N = \delta_{MN}$, and its eigenvalues are $\left(\Lambda_1, \Lambda_2, \cdots, \Lambda_6\right)$, with $\Lambda_1 \geq \Lambda_2 \geq \cdots \geq \Lambda_6 \geq 0$. The relationship between the eigenvectors $\left(\hat{\mathbf{e}}_1, \hat{\mathbf{e}}_2, \cdots, \hat{\mathbf{e}}_6\right)$ and the bases $\left(\hat{\mathbf{k}}_1, \hat{\mathbf{k}}_2, \cdots, \hat{\mathbf{k}}_6\right)$ is

$$\hat{\mathbf{e}}_M = \xi_{MN} \hat{\mathbf{k}}_N. \tag{30}$$

Then $\mathfrak{R}$ can be written as

$$\mathfrak{R} = \sum_{M=1}^{6} \Lambda_M \hat{\mathbf{e}}_M \hat{\mathbf{e}}_M. \tag{31}$$

In the eigenspace $\left(\hat{\mathbf{e}}_1, \hat{\mathbf{e}}_2, \cdots, \hat{\mathbf{e}}_6\right)$ of $\mathfrak{R}^{MN}$, $\mathbf{G}$ and $\mathbf{C}$ can be expressed as

$$\mathbf{G} = \sum_{M=1}^{6} \tilde{X}^M \hat{\mathbf{e}}_M, \tag{24''}$$

and

$$\mathbf{C} = \sum_{M=1}^{6} \tilde{C}^M \hat{\mathbf{e}}_M. \tag{26'}$$

Substituting Equations 31, 24″, and 26′ into 29′, we get

$$\Lambda_M \tilde{X}^M \hat{\mathbf{e}}_M = \tilde{C}^M \hat{\mathbf{e}}_M. \tag{32}$$

Then

$$\Lambda_M \tilde{X}^M = \tilde{C}^M. \tag{33}$$

Thus,

$$\tilde{X}^M = \frac{1}{\Lambda_M} \tilde{C}^M. \tag{34}$$

In Equation 34, it is required that $\Lambda_L > 0$. If the eigenvalue $\Lambda_L = 0$, $\tilde{X}^L$ cannot be determined. Therefore,

$$\mathbf{G} = \sum_{M=1}^{6} \tilde{X}^M \hat{\mathbf{e}}_M = \sum_{M=1}^{6} \frac{1}{\Lambda_M} \tilde{C}^M \hat{\mathbf{e}}_M = \sum_{M,N=1}^{6} \frac{1}{\Lambda_M} \tilde{C}^M \xi_{MN} \hat{\mathbf{k}}_N. \tag{35}$$

Comparing Equation 24′ and 35 leads to

$$X^N = \sum_{M=1}^{6} \frac{1}{\Lambda_M} \tilde{C}^M \xi_{MN}. \tag{36}$$

Combining Equations 26, 30, and 26′, we get

$$\tilde{C}^M = \sum_{L}^{6} \xi_{ML} C^L, \tag{37}$$

Finally, Equation 36 becomes

$$X^N = \sum_{M,L}^{6} \frac{1}{\Lambda_M} \xi_{MN} \xi_{ML} C^L, \tag{38}$$

which is the solution for the six independent components of the quadratic gradient at the barycenter of the constellation in the Earth central reference frame.

In order to obtain a more accurate quadratic gradient, an iterative method is used. The physical quantity f_c and its linear gradient $g_i = (\nabla_i f)_c$ at the barycenter are corrected by substituting the quadratic gradient G_{ij} obtained from Equation 38 into 8′ and 13. The corrected tensor c^{ij} is calculated from Equation 21. The components of the six-dimensional vector $\mathbf{C}$, $C^M = (2 - \delta_{ij}) c^{(ij)}$ are calculated. Then, the components of the quadratic gradient at the barycenter, $X^N = G_{(kl)}$ are obtained from Equation 38, which have been corrected by the first iteration. The above cycle is repeated until satisfactory accuracy is achieved. This iterative method will be tested and its reliability verified in the next section. We call this method as algorithm for the linear and quadratic gradients (ALQG), which can draw both the linear and quadratic gradients of any physical quantity from 10 or more point measurements.

The estimation of the quadratic gradient of a physical quantity relies on the configuration of the constellation. We can obtain the complete quadratic gradient if all the six eigenvalues of the characteristic matrix $\mathfrak{R}^{MN}$ are nonzero. However, as shown in Equation 38, the quadratic gradient cannot be completely determined if one or more eigenvalues of the characteristic matrix $\mathfrak{R}^{MN}$ are zero. For example, if the constellation is linearly distributed, it can be seen from Equations 16 and 27 that only the eigenvalue of the characteristic matrix $\mathfrak{R}^{MN}$ along the spacecraft array is larger than zero, while all the other five eigenvalues of the characteristic matrix $\mathfrak{R}^{MN}$ are zero. Therefore, only the quadratic gradient along the spacecraft array can be obtained in this situation. For the situation where the constellation is planar, the three eigenvalues of the characteristic matrix $\mathfrak{R}^{MN}$ along the directions in the spacecraft plane are greater than zero, while remaining three eigenvalues are zero. Thus, only the three components of the quadratic gradient in the plane of the

constellation can be found. Further investigations should be made to fully understand how the configurations of the constellations affect the determination of the quadratic gradient.

ALQG can find plenty of applications in analyzing the clustered observations at 10 or more points. For example, we can obtain the linear and quadratic gradients of the electric potential with this approach based on the potential measurements by $N \geq 10$ sensors on board one spacecraft (if they are real), and further obtain the electric field and charge density at the barycenter of the sensors. Suppose the electric potential relative to the spacecraft observed at position $\mathbf{r}_\alpha$ of the sensor α is $\phi_{(\alpha)} = \phi(\mathbf{r}_\alpha), \quad \alpha = 1,2,\cdots,N$. By using the above algorithm, we can obtain the electric potential ϕ_c and its linear and quadratic gradients, $(\nabla\phi)_c$ and $(\nabla^2\phi)_c$, at the barycenter of the constellation. Therefore, the electric field at the barycenter is

$$\mathbf{E} = -(\nabla\phi)_c. \tag{39}$$

Applying Gauss's law, we get the charge density at the barycenter as follows:

$$\rho = \varepsilon_0 (\nabla \cdot \mathbf{E})_c = -\varepsilon_0 (\nabla^2\phi)_c. \tag{40}$$

As for the multiple spacecraft magnetic field measurements, using the new algorithm (ALQG) we can obtain the magnetic linear and quadratic gradients at the barycenter of the constellation, and further obtain the complete geometry of the MFLs, including the Frenet frame, the curvature and torsion of the magnetic field lines (MFLs). Suppose that the magnetic field at position $\mathbf{r}_\alpha$ of spacecraft α is $\mathbf{B}_\alpha = \mathbf{B}(\mathbf{r}_\alpha), \alpha = 1, 2,\cdots, N$. Utilizing the above algorithm, the magnetic field and its linear gradient $(\nabla\mathbf{B})_c = \nabla\mathbf{B}(\mathbf{r}_c)$ and quadratic gradient $(\nabla\nabla\mathbf{B})_c = \nabla\nabla\mathbf{B}(\mathbf{r}_c)$ at the barycenter of the constellation can be calculated. The tangential vector or the unit magnetic vector of the MFLs is $\hat{\mathbf{b}} = \mathbf{B} / B$. The curvature of the MFLs at the barycenter of the constellation can be estimated from the following equation (Shen et al., 2003):

$$\kappa_{cj} = B_c^{-1} b_{ci} (\nabla_i B_j)_c - B_c^{-1} b_{ci} b_{cj} b_{cm} (\nabla_i B_m)_c. \tag{41}$$

The principal normal vector of the MFLs is $\hat{\mathbf{K}} = \boldsymbol{\kappa} / |\boldsymbol{\kappa}|$, and the binormal vector of the MFLs is $\hat{\mathbf{N}} = \hat{\mathbf{b}} \times \hat{\mathbf{K}}$. From its definition, $\tau \equiv (1 / \kappa)(d^2\hat{\mathbf{b}} / ds^2) \cdot \hat{\mathbf{N}}$, we can get the torsion of the MFLs at the barycenter of the constellation as the expression (Shen et al., 2020)

$$\tau_c = \kappa_c^{-1} B_c^{-3} N_{cj} B_{ci} (\nabla_i B_k)_c (\nabla_k B_j)_c + \kappa_c^{-1} B_c^{-3} N_{cj} B_{ck} B_{ci} (\nabla_k \nabla_i B_j)_c. \tag{42}$$

In this study, we have not taken advantage of the actual time series observations by the spacecraft. As explored in the work of De Keyser (2008), who made use of the time series synthetic data, fewer spacecraft are needed for determining the quadratic gradient of scalar or vector fields. The four-dimensional approach is a thorough one but is also rather complicated. Following the approach of De Keyser (2008) and combining this with the method used in this paper, a better estimator could be found for constellations with fewer than 10 spacecraft.

3. Tests

In this section, we will investigate the applicability of ALQG to the vector field, and check its ability to yield the linear and quadratic magnetic gradients and the complete geometry of the MFLs based on the multiple-point magnetic measurements.

ALQG has been tested for the cylindrical force-free flux rope, dipole magnetic field and modeled geomagnetospheric field, so as to evaluate its capabilities. Fifteen-point measurements have been assumed. The tests are focused on how well the algorithm behaves as iterations are performed and how the truncation
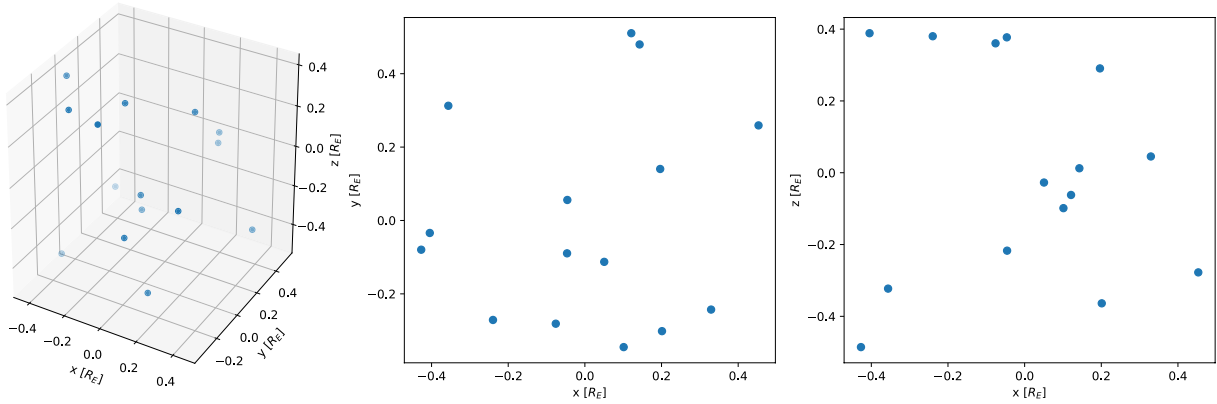
Figure 1. Schematic view of the distribution of the constellation.

errors vary with an increasing relative measurement scale. Assuming L is the size of the constellation and D is the local characteristic scale of the magnetic structure, the relative measurement scale is L/D. The influence of the number of spacecraft in the constellation on the truncation errors has also been analyzed.

3.1. Configuration of the Constellation

The positions of the 15 spacecraft of the constellation in the barycenter coordinates are generated randomly, which is shown in Figure 1. Table S1 in the Supporting Information shows the positions of the 15 spacecraft in the Cartesian coordinates in the barycenter frame. The three characteristic lengths of the constellation, a,b,c, can be defined by the square roots of the eigenvalues of the volumetric tensor R^{ij} (Harvey, 1998). For the 15-spacecraft constellation, they are $a = 0.75R_E, b = 0.61R_E, c = 0.24R_E$, and hence the size of the constellation is $L \equiv 2a = 1.5R_E$.

Based on the definition given in Equation 27, the 6×6 characteristic matrix $\mathfrak{R}^{MN}$ can be calculated as

$$\left(\mathfrak{R}^{MN}\right) = \begin{pmatrix} 9.153 & 1.887 & -0.520 & 3.523 & -3.260 & 7.683 \\ 1.887 & 14.091 & -6.52 & 2.888 & -3.32 & 1.897 \\ -0.520 & -6.52 & 30.73 & -1.66 & 3.794 & 0.5000 \\ 3.523 & 2.888 & -1.66 & 11.541 & -3.070 & 3.683 \\ -3.26 & -3.32 & 3.794 & -3.070 & 14.733 & -3.23 \\ 7.683 & 1.897 & 0.5000 & 3.683 & -3.23 & 12.016 \end{pmatrix} 10^{-3} R_E^4. \tag{43}$$

which is symmetric. Its six eigenvalues are given in Table 1, all of which are nonzero. Thus, the algorithm can be applied to calculate the linear and quadratic gradients with the measurements from this constellation. In the following tests, the configuration of the constellation will be kept unchanged, while its size will be adjusted by scaling up and down the distances between the spacecraft.

3.2. Flux Ropes

The axially symmetric force-free flux rope will be used to test the algorithm developed in Section 2. The magnetic field's cylindrical coordinates can be expressed as (Lundquist, 1950)

$$\boldsymbol{B} = B_0\left[0, J_1\left(\alpha r\right), J_0\left(\alpha r\right)\right], \tag{44}$$

Table 1
Eigenvalues (in R_E^4) of the Characteristic Matrix $\mathfrak{R}^{MN}$

Λ_1	Λ_2	Λ_3	Λ_4	Λ_5	Λ_6
0.03512	0.02385	0.002728	0.008468	0.01130	0.01080
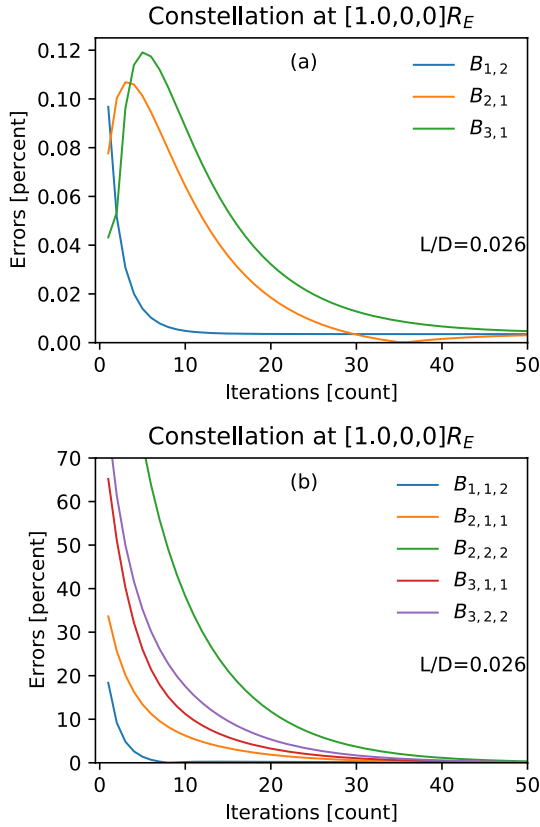
Figure 2. Relative errors of the nonvanishing components of the (a) Linear and (b) Quadratic magnetic gradients in the flux rope calculated by different numbers of iterations. It is noted that $B_{i,k} = \partial B_i / \partial x_k$, $B_{i,j,k} = \partial^2 B_i / \partial x_j \partial x_k$.

where r is the axial-centric distance, $1/\alpha$ is the characteristic scale of the flux rope, J_n is the first kind of Bessel function of order n, and B_0 is the characteristic magnetic strength in the flux rope. We can set $\alpha = 1/R_E$ and $B_0 = 60$ nT. The overall spatial characteristic scale of the flux rope is $D = 1/\alpha = 1R_E$. However, when $r < 1/\alpha = 1R_E$, it is proper to set the local characteristic scale as the axial-centric distance r, that is, $D = r$. The helix angle β of the MFLs in the cylindrical flux rope obeys $\tan \beta = J_0(\alpha r) / J_1(\alpha r)$. The curvature and torsion of the MFLs are expressed as

$$\kappa = r^{-1} \cos^2 \beta \tag{45}$$

and

$$\tau = \kappa \tan \beta, \tag{46}$$

respectively (Shen et al., 2020).

The linear and quadratic gradients of the magnetic field, $\nabla_i B_k$ and $\nabla_i \nabla_j B_k$, are usually composed of $3 \times 3 = 9$ and $6 \times 3 = 18$ independent components, respectively. The axially symmetric flux rope has two symmetries: the three components of the magnetic field in the cylindrical coordinates are invariants along both the axial and azimuthal directions. Thus, some components of the quadratic magnetic gradient are zero. It is easy to find that, the 13 independent components of $\nabla_i \nabla_j B_k$ in Cartesian coordinates at one point of the x-axis are zero, i.e., $\partial_z \partial_i B_j = 0$, and $\partial_x \partial_x B_x = \partial_y \partial_y B_x = \partial_x \partial_y B_y = \partial_x \partial_y B_z = 0$; while the remaining five independent components, $\partial_x \partial_y B_x$, $\partial_x \partial_x B_y$, $\partial_y \partial_y B_y$, $\partial_x \partial_x B_z$, and $\partial_y \partial_y B_z$ are nonzero. Similarly, for the linear magnetic gradient, $\nabla_i B_j$, its three components, $\partial_y B_x$, $\partial_x B_y$, and $\partial_x B_z$, are nonvanishing, and all the other six components are zero analytically. Without loss of generality, putting the barycenter of the constellation composed of 15 spacecraft on the x-axis, we can focus on checking the algorithm on the calculations of the five nonzero independent components of the quadratic magnetic gradient and the three nonvanishing components of the linear magnetic gradient.

We first investigate the behavior of the resultant during the iterations. Assume that the barycenter of the constellation is at $[1,0,0] R_E$, and reduce the separations between the spacecraft of the constellation proportionally so that the relative measurement scale $L/D = 0.026$. We have performed the iterative calculation and tracked the errors of the linear and quadratic gradients of the magnetic field, which are plotted in Figure 2. The relative error (vertical axis), $X_{\text{algorithm}} / X_{\text{real}} - 1$, before the first iteration is 1 for the quadratic components of the gradients since we assume that these quantities vanished at the beginning (not shown in Figure 2). After the first iteration (horizontal axis), some of the relative errors have dropped under 0.3 while others remain high. After further iterations, the errors decrease and finally converge to certain fixed values, as given by the exact solutions of the original equations. The number of iterations for the solutions to converge is varying and mostly <100. This has confirmed the convergence of the iterative method. It is noted that, in the simulations with Python (numpy) on a desktop with the Intel Core i5-6500 Quad-Core, 3,000 iterations took <1 s, which indicates the speed of this algorithm.

We then investigated the dependence of the truncation errors of the nonzero components of the linear and quadratic magnetic gradients on the relative measurement scale L/D.

We tested three situations where the barycenter of the 15-spacecraft constellation was located at three representative points, $[1,0,0] R_E$, $[0.5,0,0] R_E$, and $[0.1,0,0] R_E$ in Cartesian coordinates. We scaled up and down the size of the original 15-spacecraft constellation to adjust its characteristic size L. The algorithm was

Figure 3. Left panels (a), (c), and (e) show the relative errors of three nonvanishing components of the linear magnetic gradient and curvature (κ) of the magnetic field lines (MFLs) in the flux rope by L / D calculated for three different locations of the constellation, $[1,0,0]\,R_E$, $[0.5,0,0]\,R_E$, and $[0.1,0,0]\,R_E$ in Cartesian coordinates, respectively. Right panels (b), (d), and (f) show the relative errors of the nonvanishing components of the quadratic magnetic gradient and torsion (τ) of the MFLs in flux rope by L / D calculated for the three different locations of the constellation, $[1,0,0]\,R_E$, $[0.5,0,0]\,R_E$, and $[0.1,0,0]\,R_E$ in Cartesian coordinates, respectively. MFLs, magnetic field lines.

found to yield reliable results for most relative measurement scales L / D, where D is characteristic scale of the magnetic structure.

The calculations of the linear magnetic gradient and also the curvature of the MFLs were evaluated, which are shown in Figures 3a, 3c, and 3e. The calculated linear magnetic gradient and curvature of the MFLs have sound accuracies and their relative errors are all <5%. As shown in Figures 3a, 3c, and 3e, the relative errors of the three nonvanishing components of the linear magnetic gradient and the curvature of the MFLs vary on the second-order of L/D, which was proven by polynomial fitting. In the following, the variation in the relative errors with L/D has been verified in the same way.

As shown in Figures 3b, 3d, and 3f, the relative errors (vertical axis) of the quadratic gradients (solid lines) increase approximately linearly with L / D (horizontal axis) and are generally <5%, as do those of the resultant torsion of the magnetic field lines (dashed and dotted lines) with slightly larger errors. Note that
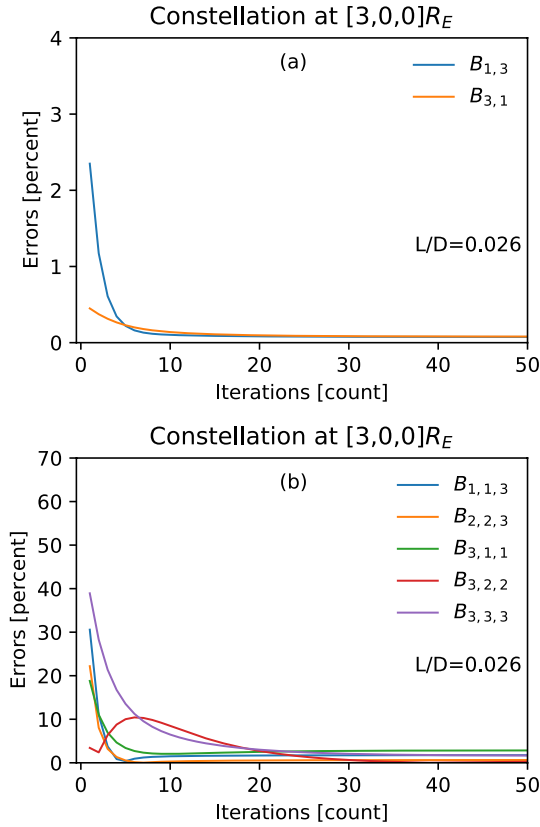
Figure 4. Relative errors of the nonvanishing components of the (a) linear and (b) quadratic magnetic gradient in the dipole field at the equatorial plane as calculated by different numbers of iterations.

all of the errors shown in Figure 3 converge. Such small errors imply that the algorithm runs well for the flux rope 15-point measurements.

Because the magnetic field in the flux rope generally varies rather smoothly in space, the application of the algorithm to it is very effective and satisfactory accuracies can be achieved as mentioned above. However, the magnetic field in space can have severe spatial variations, for example, the dipolar magnetic field. The strength of the dipolar magnetic field decreases as the third power of the distance from the dipole, and the magnetic gradients at every order are comparable. The actual calculations of the linear magnetic gradient and current density of the near-Earth magnetic field based on multiple spacecraft measurements are occasionally inaccurate (Yang et al., 2016). Here, we would like to apply the new algorithm to estimate the linear and quadratic magnetic gradients and check its accuracy and capabilities.

3.3. Dipole Magnetic Field

In this section, we will analyze the ability of the algorithm to calculate the dipole magnetic field. The dipole field in Cartesian coordinates is defined as

$$\boldsymbol{B} = \frac{M_z}{r^5}\left[3xz, 3yz, 3z^2 - r^2\right], \tag{47}$$

where M_z is the magnetic dipole moment and $r = \sqrt{x^2 + y^2 + z^2}$. It is supposed that the magnetic dipole moment points in the positive z-direction. The magnetic dipole moment is set as $M_z = -30438\,\text{nT} \cdot R_E^3$, which is approximately that of the Earth. It is easy to obtain the analytical expression for the curvature of the MFLs as

$$\kappa = \frac{3}{r}\frac{\left(1 + \cos^2\theta\right)\left|\sin\theta\right|}{\left(1 + 3\cos^2\theta\right)^{3/2}}, \tag{48}$$

where θ is the polar angle. The MFLs in the dipole magnetic field are plane curves, whose torsion is zero, that is, $\tau = 0$.

The local characteristic scale D of the magnetic field measured can be chosen to be the distance of the constellation from the dipole, that is, $D = r$.

The configuration of the constellation is the same as that in Section 3.1, which is shown in Figure 1. We scale up and down the original 15-spacecraft constellation to alter the characteristic size L of the constellation.

We investigated the convergence behavior of the components of the linear and quadratic magnetic gradients calculated by the iterative algorithm. The constellation is put at the equatorial plane of the dipole with coordinates of $[3,0,0]\,R_E$, where only five independent components of the magnetic quadratic gradient are nonzero. The separations between the spacecraft of the constellation are reduced proportionally so that the relative measurement scale $L / D = 0.026$. The convergence behaviors of the nonvanishing independent components of the linear and quadratic magnetic gradients estimated by the algorithm are shown in Figures 4a and 4b, respectively, which shows that the linear and quadratic magnetic gradients attain convergence within $\sim$50 iterations.

The algorithm was then utilized to calculate the magnetic linear and quadratic gradients as well as the curvature of the MFLs in the dipole field as expressed by Equation 47, for various characteristic scales of the
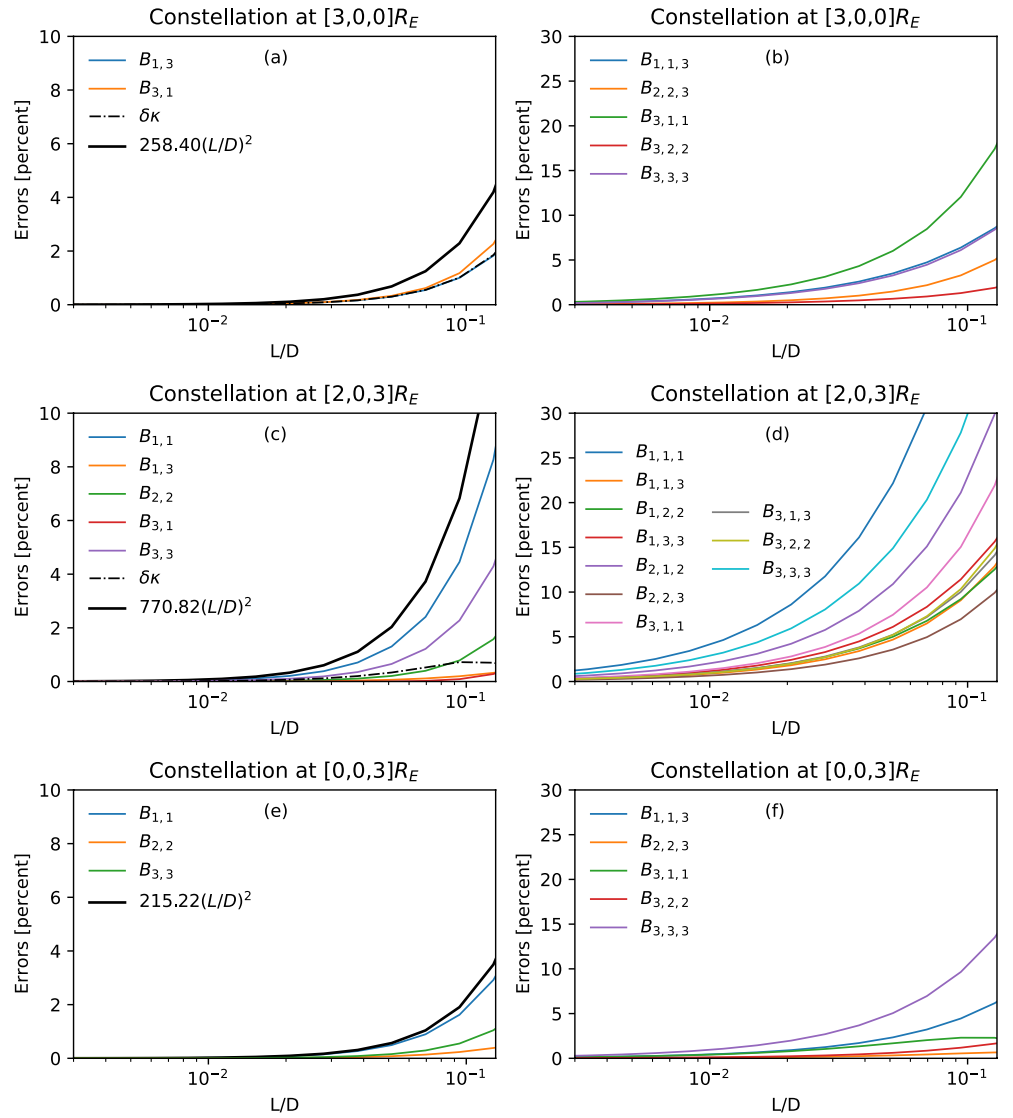
Figure 5. Left panels (a), (c), and (e) show the relative errors of the three nonvanishing components of the linear magnetic gradient and curvature (κ) of the MFLs in the dipole field by L/D calculated for three different locations of the constellation, $[3, 0, 0]R_E$, $[2, 0, 3]R_E$, and $[0, 0, 3]R_E$ in Cartesian coordinates, respectively. The solid black lines in panels (a), (c), and (e) are proportional to $\left(L/D\right)^2$, that serve as references to the second-order trends. Right panels (b), (d), and (f) show the relative errors of the nonvanishing components of the quadratic magnetic gradient in the dipole field by L/D calculated for the three different locations of the constellation, $[3, 0, 0]R_E$, $[2, 0, 3]R_E$, and $[0, 0, 3]R_E$ in Cartesian coordinates, respectively. MFLs, magnetic field lines.

constellation. The constellation is located at $\left[3,0,0\right]R_E$, $\left[2,0,3\right]R_E$, and $\left[0,0,3\right]R_E$, which correspond to low, middle, and high latitudes, respectively. As shown in Figures 5a, 5c, and 5e, the relative errors of the nonvanishing components of the linear magnetic gradient and the curvature of the MFLs are of the second-order of L/D. As $L/D < 0.01$, the relative errors of the linear magnetic gradient are <0.2%. The variations in the relative errors of the magnetic quadratic gradient calculated with the algorithm by L/D are shown in Figures 5b, 5d, and 5f. It can be seen that the relative errors of the magnetic quadratic gradients are of the first-order in L/D. However, the errors in estimating the magnetic gradients are greater than those in the case of the flux ropes. This is because the dipolar magnetic strength decreases rather rapidly with distance from the dipole. It is also shown in Figures 5b, 5d, and 5f that, as $L/D < 0.01$, the relative errors of the quadratic magnetic gradient are <5%.
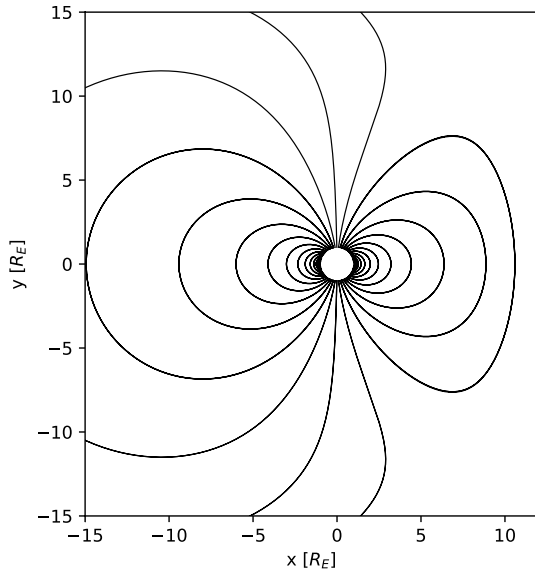
Figure 6. Magnetic field lines (MFLs) at the GSE x-z coordinate plane in the modeled magnetosphere with the magnetic field as defined in Equation 49.

3.4. Modeled Geomagnetosphere

The geomagnetic field can be assumed to include one more dipole, the mirrored dipole, in the Earth's dipole field, that is,

$$\boldsymbol{B} = \frac{M_{z1}}{r_1^5}\left[3xz, 3yz, 3z^2 - r_1^2\right] + \frac{M_{z2}}{r_2^5}\left[3\left(x - 40R_E\right)z, 3yz, 3z^2 - r_2^2\right]. \quad (49)$$

The modeled geomagnetospheric field is strongly inhomogeneous and continuously asymmetric; therefore, it serves to test algorithm more strictly and realistically. In Equation 49, M_{z1} is the Earth's dipole moment, and $r_1 = \sqrt{x^2 + y^2 + z^2}$ is the distance of the measurement point from the Earth's dipole. The mirror magnetic dipole, $M_{z2} = 28M_{z1}$, is located at $x = 40R_E$, and $r_2 = \sqrt{\left(x - 40R_E\right)^2 + y^2 + z^2}$ is the distance from the mirror dipole. The plot of the magnetic field in the modeled magnetosphere is shown in Figure 6. In general, the modeled magnetospheric field is approximately equal to the Earth's dipole field in the inner region, $r_1 \leq 6R_E$. Since the dipole field has been tested in Section 3.3, we now focus on the outer region, $r_1 > 6R_E$. Three points, $[5, 15, 5]\,R_E$, $[5, 10, 10]\,R_E$, and $[-5, 15, 10]\,R_E$, corresponding to the far flank and high latitude at dayside and high latitude far flank at nightside, respectively, are chosen as the locations of the barycenter. Here, we define the relative errors of the components $\partial_j B_i$ and $\partial_k \partial_j B_i$ as

$$e_{ij} = \frac{\left(\partial_j B_i\right)_{\text{algorithm}} - \left(\partial_j B_i\right)_{\text{real}}}{\langle \partial B \rangle}, \quad (50)$$

and

$$e_{ijk} = \frac{\left(\partial_k \partial_j B_i\right)_{\text{algorithm}} - \left(\partial_k \partial_j B_i\right)_{\text{real}}}{\langle \partial \partial B \rangle}, \quad (51)$$

respectively, where $\langle \partial B \rangle = \sum_{i,j}^{3}\left|\partial_j B_i\right| / 9$ and $\langle \partial \partial B \rangle = \sum_{i,j,k}^{3}\left|\partial_k \partial_j B\right|_i / 27$ are the average values of the components of the linear and quadratic magnetic gradients, respectively.

Figure 7 shows the convergent trend of the linear and quadratic gradients within 50 iterations when the separation between the spacecraft in the constellation is adjusted to make $L / D = 0.026$. By iteration we can obtain the true solutions of the set of equations (estimators) of the algorithm. However, because the algorithm has omitted the terms higher than second-order the exact solutions of the set of equations contain truncation errors (which are evident in Figure 7). Again the algorithm is confirmed to be reliable and suitable for analyzing fields varying severely in space.

Figure 8 shows the relative errors of all components of the linear and quadratic gradient calculated at different spacecraft scales and locations. Due to the inhomogeneity and asymmetry of the geomagnetospheric field, all components are nonvanishing. It is found that the linear gradients increase quadratically with L / D and the quadratic gradients linearly with L / D. As $L / D < 0.01$, the relative errors of the quadratic gradients are below 10%, and those of the linear gradients are below $\sim 2\%$. The accuracy of the algorithm for the modeled magnetospheric field is close to that for the dipole field.

The global geometry of the magnetospheric magnetic field can also serve as an elaborate scenario for testing. The geometrical features of the MFLs can commonly be depicted by the curvature κ and torsion τ. On the other hand, they can also be represented by another set of parameters, the radius of curvature and the spiral angle, (R_c, β). We have compared the analytical distributions of the radius of curvature and spiral angle of MFLs in the $x = 0$ plane and those calculated based on the algorithm, and the re-
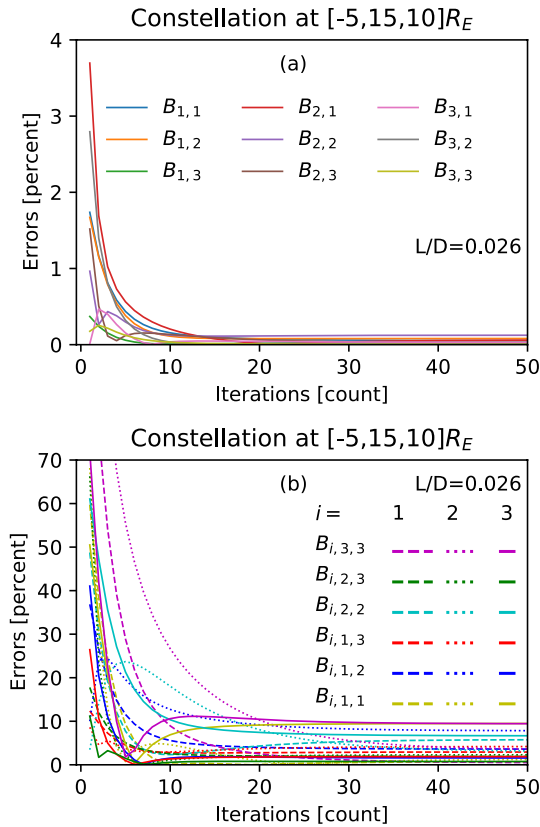
Figure 7. Relative errors of the components of the (a) linear and (b) quadratic magnetic gradients in the modeled geomagnetic field at the position $[-5, 15, 10] R_E$ as calculated by different numbers of iterations. The scale of the constellation is set as $L / D = 0.026$. In panel (b), the colored dashed, dotted, and solid lines are for derivatives of B_1, B_2, and B_3, respectively.

sults are shown in Figure 9. Note that we have only modeled the region with ($y > 0, z > 0$), one-quarter of the magnetosphere, on considering the north-south and dawn-dusk symmetries of the modeled magnetosphere. Analytically, the modeled geomagnetic field has mirror symmetry about the $z = 0$ coordinate plane (or the equatorial plane), so that the torsion of the MFLs is negated through the mirror and is zero at the equatorial plane with $z = 0$, as indicated in panel (c) of Figure 9. The separation between the spacecraft is fixed at $L = 28$ km. With the ever-changing D when we move the constellation around, the largest relative scale is $L / D = 0.0545$ at bottom-left corner (near the Earth), while the least scale $L / D = 0.00400$ at top-right corner. The radius of curvature given by the algorithm is almost identical to its real value, as shown in the top panels of Figure 9. The MFLs tend to be straighter at the polar regions and more bending at the low-latitude regions. The distribution of the spiral angles of the MFLs, as obtained by the algorithm, is shown in panel (d) of Figure 9, which is consistent with that calculated analytically, as shown in panel (c). Both of them show the strong twist of the MFLs in the duskside cusp region. It is noted that at the low-attitude polar region, the algorithm yields negative spiral angles of the MFLs, as shown in the deep-blue area in panel (d). This abnormal deviation from the accurate calculation results mainly from the extremely small curvature of the MFLs in this region. Figures S1–S3 in the Supporting Information present plots of the distributions of the radius of curvature and helix angle of MFLs in three other coordinate planes in modeled magnetosphere based on theoretical and new algorithm calculations and thus to further illustrate the ability of the new algorithm.

In this test, 15 measurement points were applied and we have verified the feasibility and accuracy of ALQG. The algorithm needs at least 10 measurement points as input to estimate the quadratic gradient reliably. The more points the algorithm builds on, the more accurate the estimated quadratic gradients are.

To investigate this relationship, we need to exclude the effect of the spatial distribution of the constellation. For the n points used for modeling, we generated 1,000 constellations spontaneously, each consisting of n spacecraft, and then chose one constellation with a minimum error of the calculation as the representative case. Figure 9 shows the mean relative errors of the linear and quadratic magnetic gradients at $[1,1,2] R_E$ in the modeled magnetospheric field derived from virtual measurements of constellations with different numbers of spacecraft n and two fixed characteristic spatial scales L / D. As indicated by the dashed magenta lines, the mean error of the quadratic gradient is nearly proportional to $1 / n$. The mean error of the linear gradient, however, appears to be a constant plus a weak variation of the number of spacecraft in the constellation. The averaged mean error of the linear magnetic gradient is about $2.07 \times 10^{-1}\%$ for $L / D = 0.05$ and $8.28 \times 10^{-3}\%$ for $L / D = 0.01$. As indicated by Figure 10, the results obtained here also confirm the previous arguments that the errors of the linear gradient components decrease quadratically with L / D and those of the quadratic gradient components linearly with L / D (see Figure 10).

The convergence of the iteration was not verified mathematically in this study. However, it was found that the iterations led to convergence in all of the more than 10,000 simulations we carried out for the three vector field models with constellations of random configurations and different numbers of spacecraft.

In the actual measurement data, there are usually noises and turbulences, that will possibly lead to additional errors besides the truncation errors in the calculations. In the simulations, it is found that the noises do not affect the convergence of the iterations. Nevertheless, a white noise would affect the accuracy of the algorithm at much lower L / D when the difference between the measured values from different
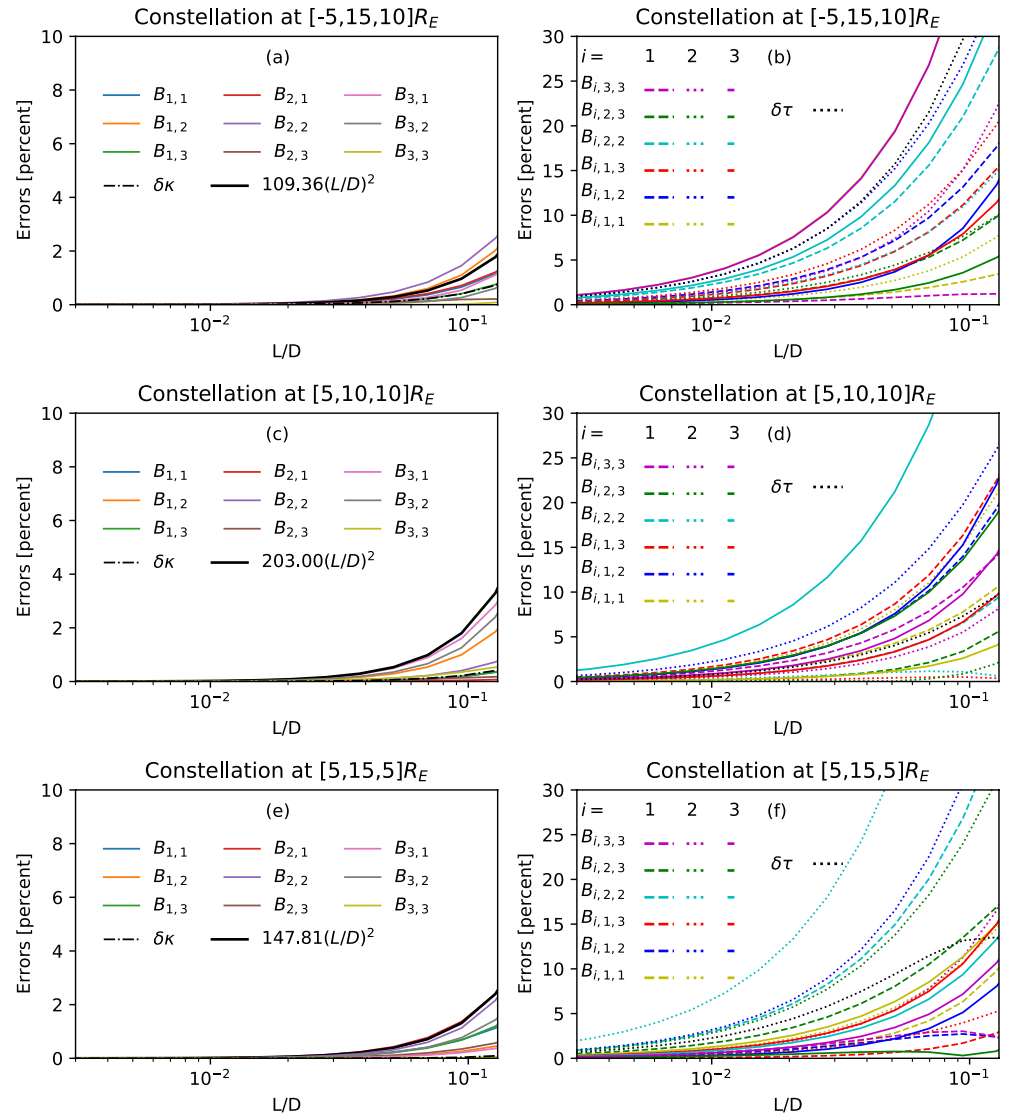
Figure 8. Left panels (a), (c), and (e) show the relative errors of the components of the linear magnetic gradient and curvature (κ) of the MFLs in the geomagnetic field by L / D calculated at three different locations of the constellation, $[-5, 15, 10] R_E$, $[5, 10, 10] R_E$, and $[5, 15, 5] R_E$ in Cartesian coordinates, respectively. The black dash-dotted line is for the curvature. The solid black lines in panels (a), (c), and (e) are proportional to $\left(L / D \right)^2$, that serve as references to the second-order trends. Right panels (b), (d), and (f) show the relative errors of the components of the quadratic magnetic gradient and torsion (τ) of the MFLs in magnetospheric field by L / D calculated for the three different locations of the constellation, $[-5, 15, 10] R_E$, $[5, 10, 10] R_E$, and $[5, 15, 5] R_E$ in Cartesian coordinates, respectively. The black dotted line is for the torsion. MFLs, magnetic field lines.

spacecrafts is close to the measurement errors. Disturbances take similar effects but can be reduced easily by wave filters in actual applications (Shen et al., 2020). Presently, we still have no actual observation data while the main goal of this work is to derive the algorithm. So that this problem can be investigated in detail late.

In this section, we have focused on confirming the feasibility of the general algorithm. Therefore, in all the above three tests on magnetic fields, we have not taken advantage of the physical constraints, for example, the divergence-free condition of the magnetic field, that is, $\nabla \cdot \mathbf{B} = 0$. With this constraint, the number of spacecraft in the constellation can still be reduced.
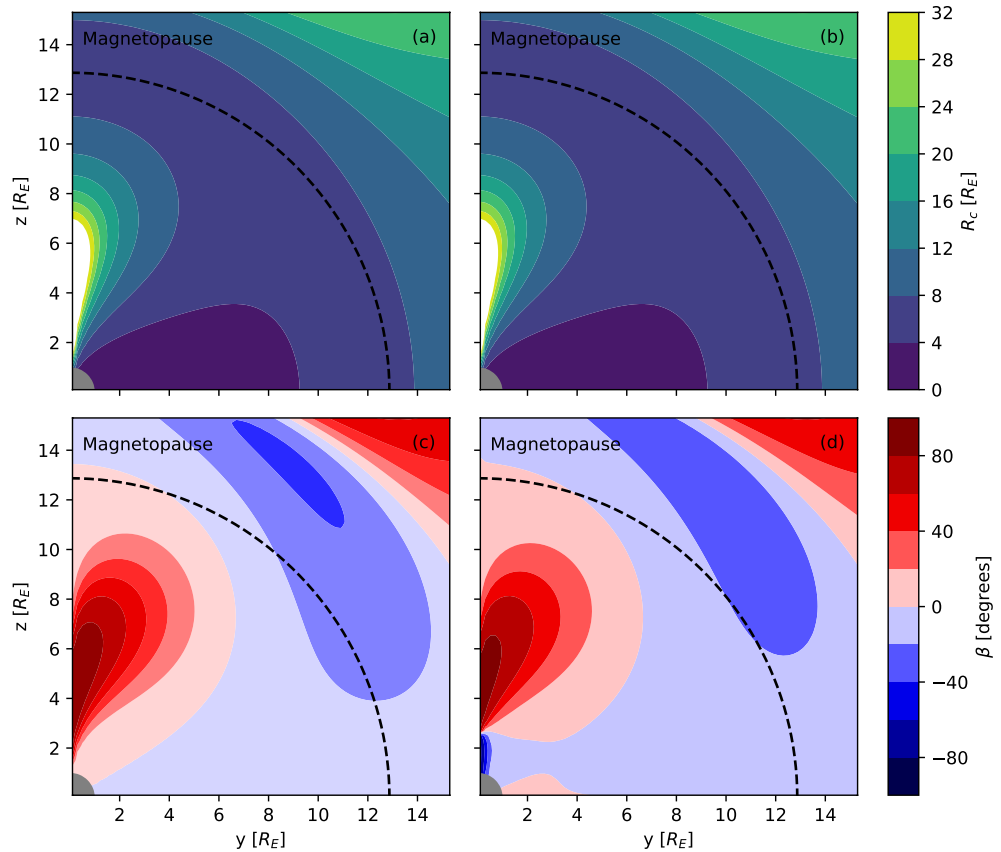
Figure 9. Distributions of the radius of curvature (top) and helix angle (bottom) of MFLs in the coordinate plane $x = 0$ in modeled magnetosphere based on theoretical (left) and new algorithm (right) calculations. The dashed line indicates the magnetopause when $B_z = 27\,\mathrm{nT}$, $D_p = 3\,\mathrm{nPa}$ (Shue et al., 1998). The white color in panels (a) and (b) represent radius of curvature of MFLs greater than $32 R_E$. MFLs, magnetic field lines.

4. Summary and Conclusion

The algorithms for calculating the linear gradients of physical quantities based on the measurements by constellations composed of four or more spacecraft have been well established and have found wide applications in Cluster, THEMIS, and MMS data analyses. With the evolution of space explorations, 10 or more spacecraft constellations will be quite feasible in the near future. Therefore, it is meaningful to develop the method to draw the high order gradients of the physical quantities based on ≥10 point measurements so as to adequately prepare for future multiple-point data analysis.
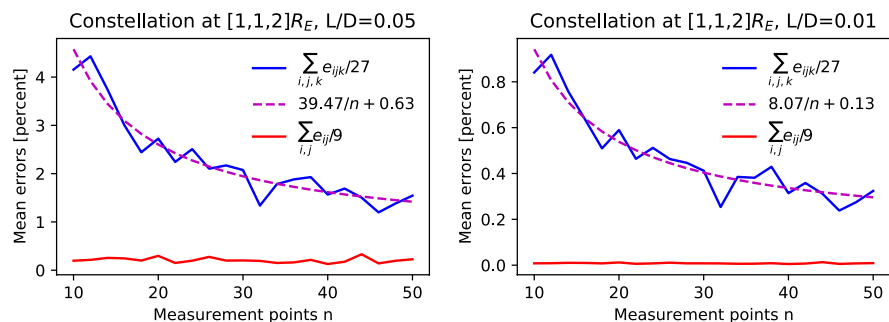
Figure 10. Mean truncation errors of linear (red) and quadratic (blue) gradients for different numbers of measurement points. The modeling is for $L / D = 0.05$ (left) and $L / D = 0.01$ (right) at $[1,1,2] R_E$ in the modeled magnetosphere. The dashed magenta line is a fitted curve.

In this investigation, we have established an algorithm (ALQG) to deduce both the linear and quadratic gradients of an arbitrary physical quantity using the least squares method. This approach can yield the linear and quadratic gradients at the barycenter of a constellation with an input of ≥10 measurement points. Using the least squares method, the equations for determining the physical quantity and its linear and quadratic gradients at the barycenter have been found. To solve these equations, iterations are made in order to find the approximation solutions. First, under the linear approximation, the linear gradient is obtained from the multiple-point measurements. Then, the quadratic gradient is calculated on these bases. Finally, the first iteration is carried out and the quantity and its linear gradient at the barycenter are modified by the quadratic gradient obtained. The quadratic gradient is then recalculated with the corrected values of the physical quantity and its linear gradient. The iterations are performed until the linear and quadratic gradients with satisfactory accuracies have been obtained.

Generally, the determination of the three components of the linear gradient of a physical quantity is dependent of the 3×3 volume matrix that reflects the configuration of the constellation (Chanteur, 1998; Harvey, 1998). This exploration indicates that the calculations of the six independent components of the quadratic gradient rely on the 6×6 symmetric characteristic matrix $\Re^{MN}$ of the constellation. If the six eigenvalues of the characteristic matrix $\Re^{MN}$ are all nonzero, the six components of the quadratic gradient can be fully determined.

Using 10-point electric potential observations, the linear and quadratic gradients at the barycenter can be found, as well as the electric field and charge density. Using 10-point magnetic field measurements, the linear and quadratic magnetic gradients at the barycenter can be obtained, as well as the complete geometry of the MFLs.

Tests on ALQG were carried out using the cylindrical flux ropes, the dipole magnetic field, and the modeled geomagnetospheric field, and the reliability and accuracy of the algorithm were confirmed. In these tests, the spatial distribution of the geometrical parameters (radius of curvature and spiral angle) of the MFLs in the modeled geomagnetospheric field were also obtained, which were in good agreement with the analytic results. All three tests showed that, the calculations converged within 50 iterations. The obtained linear gradient was of second-order accuracy, while the quadratic gradient was of first-order accuracy. The results of the test on the modeled geomagnetospheric field indicated that increasing the number of spacecraft in the constellation can enhance the accuracy of the calculated quadratic gradient and that its relative errors are inversely proportional to the number of spacecraft. However, the accuracy of the linear gradient obtained cannot be further improved by increasing the number of the spacecraft, and its relative errors are almost independent of the number of the spacecraft. Thus, the algorithm we have developed is a very effective, reliable and accurate one for jointly calculating both the linear and quadratic gradients of various physical quantities with ≥10-point constellation measurements.

This approach can be used to calculate the complete geometrical parameters of the magnetic field (e.g., the curvature and torsion of the MFLs) in the magnetosphere (e.g., with Tsyganenko models) numerically. This algorithm is also very meaningful for the design of future multiple spacecraft missions. For a constellation with 10 or more spacecraft, its characteristic matrix $\Re^{MN}$ needs to have six nonzero eigenvalues in order to enable the complete determination of the quadratic gradients of the physical quantities. This algorithm will therefore find wide applications in the analysis of multiple-point observation data.

Data Availability Statement

No observation data have been used in this investigation. The codes for the algorithm are available at the website: http://doi.org/10.5281/zenodo.4636552 or https://github.com/SpaceWalker162/quadraticGradient/tree/master.

References

Burch, J. L., Moore, T. E., Torbert, R. B., & Giles, B. L. (2016). Magnetospheric multiscale overview and science objectives. *Space Science Reviews*, *199*(1–4), 5–21. https://doi.org/10.1007/s11214-015-0164-9

Chanteur, G. (1998). Spatial interpolation for four spacecraft: Theory. In G. Paschmann, & P. W. Daly (Eds.), *Analysis methods for multi-spacecraft data* (p. 349). Noordwijk: ESA Publication Division.

De Keyser, J. (2008). Least-squares multi-spacecraft gradient calculation with automatic error estimation. *Annales Geophysicae*, *26*(11), 3295–3316. https://doi.org/10.5194/angeo-26-3295-2008

De Keyser, J., Dunlop, M. W., Darrouzet, F., & Dècrèau, P. M. E. (2007). Least-squares gradient calculation from multi-point observations of scalar and vector fields: Methodology and applications with cluster in the plasmasphere. *Annales Geophysicae*, *25*, 971–987. https://doi.org/10.5194/angeo-25-971-2007

Dunlop, M. W., Southwood, D. J., Glassmeier, K.-H., & Neubauer, F. M. (1988). Analysis of multipoint magnetometer data. *Advances in Space Research*, *8*, 273. https://doi.org/10.1016/0273-1177(88)90141-x

Hamrin, M., Rönnmark, K., Börlin, N., Vedin, J., & Vaivads, A. (2008). Gals—Gradient analysis by least squares. *Annales Geophysicae*, *26*(11), 3491–3499. https://doi.org/10.5194/angeo-26-3491-2008

Harvey, C. C. (1998). Spatial gradients and the volumetric tensor. In G. Paschmann, & P. W. Daly (Eds.), *Analysis methods for multi-spacecraft data* (p. 307). Noordwijk, The Netherlands: ESA Publications Division.

Liu, Y. Y., Fu, H. S., Olshevsky, V., Pontin, D. I., Liu, C. M., Wang, Z. et al. (2019). SOTE: A nonlinear method for magnetic topology reconstruction in space plasmas. *The Astrophysical Journal-Supplement Series*, *244*, 31. https://doi.org/10.3847/1538-4365/ab391a

Lundquist, S. (1950). Magnetohydrostatic fields. *Arkiv for Fysik*, *2*, 361–365.

Pollock, C., Moore, T. E., Jacques, A., Burch, J., Gliese, U., Saito, Y., et al. (2016). Fast plasma investigation for magnetospheric multiscale. *Space Science Reviews*, *199*(1–4), 331–406. https://doi.org/10.1007/s11214-016-0245-4

Russell, C. T., Anderson, B. J., Baumjohann, W., Bromund, K. R., Dearborn, D., Fischer, D., et al. (2016). The magnetospheric multiscale magnetometers. *Space Science Reviews*, *199*(1–4), 189–256. https://doi.org/10.1007/s11214-014-0057-3

Shen, C., Li, X., Dunlop, M., Liu, Z. X., Balogh, A., Baker, D. N., et al. (2003). Analyses on the geometrical structure of magnetic field in the current sheet based on cluster measurements. *Journal of Geophysical Research*, *108*(A5), 1168. https://doi.org/10.1029/2002JA009612

Shen, C., Zhang, C., Rong, Z. J., Pu, Z. Y., Dunlop, M., Escoubet, C. P., et al. (2020). The quadratic magnetic gradient and complete geometry of magnetic field lines deduced from multiple spacecraft measurements. In Earth and Space Science Open Archive. Copernicus Meetings. https://doi.org/10.1002/essoar.10504683.1

Shue, J.-H., Song, P., Russell, C. T., Steinberg, J. T., Chao, J. K., Zastenker, G., et al. (1998). Magnetopause location under extreme solar wind conditions. *Journal of Geophysical Research*, *103*, 17691–17700. https://doi.org/10.1029/98JA01103

Torbert, R. B., Dors, I., Argall, M. R., Genestreti, K. J., Burch, J. L., Farrugia, C. J., et al. (2020). A new method of 3-D magnetic field reconstruction. *Geophysical Research Letters*, *47*, e2019GL085542. https://doi.org/10.1029/2019GL085542

Vogt, J., Albert, A., & Marghitu, O. (2009). Analysis of three-spacecraft data using planar reciprocal vectors: Methodological framework and spatial gradient estimation. *Annals of Geophysics*, *27*, 3249–3273. https://doi.org/10.5194/angeo-27-3249-2009

Vogt, J., Paschmann, G., & Chanteur, G. (2008). Reciprocal vectors. In G. Paschmann, & P. W. Daly (Eds.), *Multi-spacecraft analysis methods revisited, ISSI Sci. Rep., SR-008* (pp. 33–46). Dordrecht: Kluwer Academic.

Yang, Y. Y., Shen, C., Dunlop, M., Rong, Z. J., Li, X., Angelopoulos, V., et al. (2016). Storm time current distribution in the inner equatorial magnetosphere: THEMIS observations. *Journal of Geophysical Research: Space Physics*, *121*, 5250–5259. https://doi.org/10.1002/.2015JA022145